Evaluating Twenty-Year Trends in Earth's Energy Flows from Observations

Norman G. Loeb[1*], Michael Mayer[2,3], Seiji Kato[1], John T. Fasullo[4], Hao Zuo[2], Retish Senan[2], John M. Lyman[5,6], Gregory C. Johnson[5] and Magdalena Balmaseda[2]

[1]NASA Langley Research Center, Hampton, VA 23681, USA

[2]European Centre for Medium-Range Weather Forecasts, Reading, UK

[3]Department of Meteorology and Geophysics, University of Vienna, Vienna, Austria

[4]Climate and Global Dynamics Division, National Center for Atmospheric Research, Boulder, CO

[5]NOAA/Pacific Marine Environmental Laboratory, Seattle, WA, USA

[6]Cooperative Institute for Marine and Atmospheric Research, University of Hawaii at Manoa, Honolulu, HI, USA

Key Points:

- Regional and global trends in top-of-atmosphere net radiation from atmospheric reanalyses differ markedly from satellite observations
- Indirect and direct methods for determining divergence of atmospheric energy transport and surface flux yield similar trend patterns
- Observing system changes and model bias in atmospheric and oceanic reanalyses remain a challenge for accurate trend determination
- Our results highlight a central role for well-calibrated satellite observations in establishing trend patterns in nature
- Robust trends are observed over the Gulf Stream associated with enhanced surface-to-atmosphere heat flux

* Corresponding Author: Norman G. Loeb, norman.g.loeb@nasa.gov; NASA Langley Research Center, Hampton, VA 21 Langley Boulevard, Hampton, VA 23681

Abstract

Satellite, reanalysis, and ocean in situ data are analyzed to evaluate regional, hemispheric and global mean trends in Earth's energy fluxes during the first twenty years of the 21st century. Regional trends in net top-of-atmosphere (TOA) radiation from the Clouds and the Earth's Radiant Energy System (CERES), ECMWF Reanalysis 5 (ERA5), and a model similar to ERA5 with prescribed sea surface temperature (SST) and sea ice differ markedly, particularly over the Eastern Pacific Ocean, where CERES observes large positive trends. Hemispheric and global mean net TOA flux trends for the two reanalyses are smaller than CERES, and their climatological means are half those of CERES in the southern hemisphere (SH) and more than nine times larger in the northern hemisphere (NH). The regional trend pattern of the divergence of total atmospheric energy transport (TEDIV) over ocean determined using ERA5 analyzed fields is similar to that inferred from the difference between TOA and surface fluxes from ERA5 short-term forecasts. There is also agreement in the trend pattern over ocean for surface fluxes inferred as a residual between CERES net TOA flux and ERA5 analysis TEDIV and surface fluxes obtained directly from ERA5 forecasts. Robust trends are observed over the Gulf Stream associated with enhanced surface-to-atmosphere transfer of heat. Within the ocean, larger trends in ocean heating rate are found in the NH than the SH after 2005, but the magnitude of the trend varies greatly among datasets.

1. Introduction

Earth's energy flows encompass the exchange of energy between Earth and space and between Earth's atmosphere, ocean, lithosphere, and cryosphere. These exchanges occur over a range of time and space scales and influence weather and climate at any given location and time. A thorough understanding of Earth's energy flows is thus necessary in order to project how regional and global climate will change in response to radiative forcing. Observations of Earth's energy flows are essential for evaluating and improving the climate models used to make these projections. Ideally, the observations must provide accurate descriptions of the mean state of Earth's energy flows as well as their variations on seasonal, interannual, and decadal time scales.

Efforts aimed at quantifying Earth's mean energy flows date back to the early 20th century (Hunt et al., 1986). So-called "radiation budget diagrams" of global mean values of shortwave and longwave radiation within the climate system first appeared in 1908 (Abbot and Fowle, 1908 a, b). These diagrams were later extended to include non-radiative contributions (Dines, 1917; London, 1957). Energy budget diagrams were further refined following the launch of the first orbiting satellites, which included instruments designed to observe Earth's radiation budget (ERB; House et al., 1986). A key advance was made by Keihl and Trenberth (1997), who used adjusted global mean top-of-atmosphere (TOA) radiative fluxes from the Earth Radiation Budget Experiment (ERBE), surface radiative fluxes derived from radiative transfer calculations, surface latent heat flux inferred from estimates of global mean precipitation, and sensible heat flux determined as a residual ensuring a global energy balance at the surface. Subsequent studies by Trenberth et al. (2009), Stephens et al. (2012), Wild et al. (2013) and L'Ecuyer et al. (2015) further refined the global mean energy budget diagram using increasingly more sophisticated datasets and analysis techniques.

Early efforts aimed at quantifying energy transports within the climate system focused primarily on meridional transports (e.g., Vonder Haar and Oort 1973; Oort and Vonder Haar 1976; Trenberth 1979) using satellite observations to determine the required total energy transport and radiosonde data to determine the atmospheric transports. The ocean transport was then computed as a residual. Alternately, the ocean heat transport was also determined directly using hydrographic cross sections of temperature and salinity (Bryan, 1982). However, both approaches suffered from large sampling errors due to lack of data coverage over the oceans. The use of reanalysis combined with satellite observations of ERB for determining atmospheric and oceanic transports significantly reduced sampling error (Masuda, 1988; Trenberth and Caron, 2001), leading to more reliable results compared to the earlier studies. Furthermore, Trenberth and Fasullo (2017) show that surface fluxes derived as a residual between satellite TOA net downward radiation and estimates of the divergence of the vertically integrated atmospheric energy from reanalysis overcome many of the known issues in determining surface flux directly—such as near-surface meteorological variables and bulk flux parameterizations (Yu et al., 2019).

The combination of ERB satellite and atmospheric reanalysis has been used not only to study the global mean energy budget and mean meridional transports but also their annual cycles and land-ocean exchanges (Fasullo and Trenberth, 2008a,b), cross-equatorial heat transports (Trenberth and Fasullo, 2008; Donahoe et al., 2013; Frierson et al., 2013; Marshall et al., 2013; Loeb et al., 2015; Mayer et al., 2017; Liu et al., 2020), as well as El Niño–Southern Oscillation (ENSO) and other interannual variability (Loeb et al., 2014; Mayer et al. 2014; Trenberth and Fasullo, 2017). Recently, refinements have been made to the formulation of the atmospheric energy budget to include contributions from vertical enthalpy fluxes at the surface associated with precipitation and evaporation (Mayer et al., 2017; Trenberth and Fasullo, 2018; Kato et al., 2021).

It has recently been demonstrated that TOA ERB data from the Clouds and the Earth's Energy System (CERES) provide robust trends since 2000 (Loeb et al., 2021). At the same time, there has been tremendous progress made in atmospheric and ocean reanalysis systems, with new versions seeing improvements over their predecessors as a result of updates to the underlying model, assimilation system and input data stream (Dee et al. 2014; Buizza et al. 2018; Hersbach et al. 2020; Gelaro et al., 2017; Storto et al., 2019; Zuo et al., 2019, 2021).

A question that has yet to be addressed in detail is to what extent can we trust multi-decadal time-scale trends in different components of Earth's energy budget and energy flows within the climate system. Here "trend" refers to the relatively short 20-year period since 2000, which is likely influenced by both anthropogenic forcing and internal variability (Raghuraman et al., 2021). We do not expect that these trends are necessarily representative of longer-term trends, though aspects have been tied to climate change (e.g. Hartmann and Ceppi 2014). Rather our goal is to investigate the strengths and weaknesses of using observation based data to determine trends in TOA radiation, atmospheric energy transport, surface flux, and ocean heating rate. The latter is determined from the tendency in OHCA. While evaluations of atmospheric reanalyses for trends in atmospheric moisture transport (Trenberth et al., 2011) and latent heat flux (Robertson et al., 2020) have been conducted, similar analyses for other components of Earth's energy budget are lacking.

We limit our investigation to satellite observations from CERES, atmospheric and oceanic reanalysis from the European Centre for Medium-Range Weather Forecasts (ECMWF), and ocean heating rate calculations benefiting from data collected by the revolutionary Argo array of profiling floats (mapped alone, mapped in combination with sea-surface height data from satellite altimeters, and assimilated into reanalyses). The limited number of datasets used enables a more

focused assessment of the impact data assimilation in reanalysis on trends. In addition, to our knowledge, ECMWF data are the only source that have been used to calculate the divergence of lateral atmospheric energy transports using the most recent methodological advances (Mayer et al., 2021). The datasets used in the analysis are described in Section 2. This is followed by a description of the methodology applied to the data in Section 3, and results are presented in Section 4. A summary of our main findings are provided in Section 5.

2. Data

We use TOA and surface radiation fields from CERES and ECMWF reanalyses, total atmospheric energy transport estimates from those same ECMWF reanalyses, as well as ocean heating rate estimates derived from two different ECMWF ocean reanalyses, an observational product combining Argo temperature profiles with sea-surface height maps from satellite altimeters, and an Argo-only observational product.

2.1 CERES TOA and Surface Radiation Data

Satellite radiation data are from the CERES Energy Balanced and Filled (EBAF) Ed4.1 product (Loeb et al., 2018a), which provides monthly mean TOA and surface shortwave (SW), longwave (LW), net (NET) radiative fluxes and solar irradiance measurements on a 1°×1° grid along with imager-derived cloud properties. TOA absorbed solar radiation (ASR) is determined from the difference between spatially and temporally averaged monthly solar irradiances and reflected SW fluxes. The solar irradiances are determined from time-varying instantaneous total solar irradiance measurements from various sources (Loeb et al., 2018). Satellite incoming and outgoing radiative fluxes are presently not at the level of accuracy required to resolve TOA fluxes to a few tenths of a Wm^{-2} in an absolute sense (Loeb et al., 2018). However, CERES TOA fluxes

144 are highly precise as the instruments are very stable (Loeb et al., 2016; Loeb et al., 2018b; Shankar
145 et al., 2020; Loeb et al., 2021). The EBAF product uses an objective constrainment algorithm
146 (Loeb et al., 2009) to adjust SW and LW TOA fluxes within their ranges of uncertainty to remove
147 the inconsistency between average global net TOA flux and heat storage in the earth–atmosphere
148 system, determined primarily from ocean heat content anomaly (OHCA) data (Johnson et al.,
149 2016). Use of this approach to anchor the satellite EEI to the in situ EEI does not affect the
150 variability and trends in the data.

151 We also use TOA fluxes from the Terra and Aqua CERES SSF1deg Ed 4.1 products
152 (Doelling et al., 2013; Loeb et al., 2018a) in order to compare CERES fluxes from different satellite
153 platforms. Unlike CERES EBAF, which combines CERES instruments on different satellites,
154 SSF1deg is determined separately for each satellite CERES instruments fly on. The CERES
155 SSF1deg product is derived directly from the CERES Single Scanner Footprint TOA/Surface
156 Fluxes and Clouds (SSF) Level 2 product, which consists of instantaneous footprint-level fluxes.

157 Two sources of surface radiation are considered. The first is from the CERES EBAF Ed4.1
158 product (Kato et al., 2018) and the second is Aqua-only SYN1deg-Month. EBAF Ed4.1 surface
159 fluxes are derived by making adjustments to the inputs used to compute all-sky and clear-sky
160 surface fluxes in SYN1deg Ed4.1 (Rutan et al., 2015). The adjustments ensure that computed and
161 EBAF-observed TOA radiative fluxes agree to within observational uncertainty. The modified
162 inputs are then used to derive surface radiative fluxes that are self-consistent with the observed
163 EBAF TOA fluxes. The SYN1deg surface radiative fluxes are determined from radiative transfer
164 model calculations initialized using cloud inputs from the Moderate Resolution Imaging
165 Spectroradiometer (MODIS) instruments aboard the Terra and Aqua satellite platforms and hourly
166 geostationary (GEO) imager data between 60°S-60°N, atmospheric state inputs from the Goddard

Earth Observing System (GEOS), version 5.4.1, reanalysis (Rienecker et al. 2008), surface albedo inputs from Rutan et al. (2009), and aerosol inputs based upon an updated version of the assimilation system described in Collins et al. (2001).

Because trends in surface radiative fluxes derived using cloud information from GEO imagers are impacted by changes in the design and quality of the GEO instruments over the CERES period (Doelling et al., 2013; Kato et al., 2018), we also determine surface fluxes using a modified version of SYN1deg, which we refer to as Aqua-only SYN1deg-Month. This version uses the same atmospheric state and surface property inputs as Terra+Aqua+GEO SYN1deg-Month, but replaces the GEO cloud properties with those derived from MODIS-Aqua only (Minnis et al., 2020). Instantaneous MODIS cloud retrievals are averaged into 1°×1° grid boxes. MODIS-Aqua provides cloud properties twice a day for most of non-polar grid boxes. Hourly daytime cloud properties for a grid box are derived by interpolating daytime cloud properties from MODIS across days within a month for the grid box (Doelling et al, 2013). Hourly nighttime properties for a grid box are derived in a similar manner using nighttime MODIS cloud properties. In addition, daytime or nighttime monthly mean cloud properties are used for all hours before the first MODIS observations in the month and after the last MODIS observations in the month. That is, there is no interpolation of cloud properties across different months. In addition, the MATCH aerosol transport model used in Aqua-only SYN1deg-Month only assimilates aerosol optical thickness derived from MODIS Aqua as opposed to both Terra and Aqua for Terra+Aqua+Geo SYN1deg-Month. Aqua-only surface net shortwave and longwave flux trend plots are determined using anomalies for August 2002-February 2020 since that is the period for which Aqua-only SYN is available.

2.2 ERA5 and Integrated Forecasting System (IFS) AMIP

ERA5 is the most recent atmospheric reanalysis effort by ECMWF (Hersbach et al., 2020). It provides global data on an N320 Gaussian grid (equivalent to 0.288° spatial resolution) at 1-hourly temporal resolution in 137 atmospheric levels up to a pressure of 0.01 hPa. ERA5 is currently available from 1979 onward and consists of analyses and shortrange forecasts. The analyses are a physically consistent blend of observations and a short-range forecast based upon the previous analysis. Shortrange forecasts are initialized from the analyzed fields daily at 0600 and 1800 UTC. ERA5 uses forcing files from CMIP5 through 2005 and Representative Concentration Pathways 2.6 (RCP2.6) for 2006-2020 (Hersbach et al., 2015, 2020).

Here we use profiles of hourly ERA5 analyses of atmospheric wind, temperature, and humidity to calculate vertically integrated divergence of total atmospheric energy transport (TEDIV; Section 3.1). We also consider ERA5 short-term forecasts of TOA and surface radiative fluxes as well as surface turbulent heat fluxes for a check on model fidelity.

The IFS AMIP is a continuous atmospheric model integration with a similar setup as ERA5, but uses a slightly newer model cycle. It is initialized in March 2000 and integrated until the end of February 2020 without data assimilation, but with prescribed SSTs and sea ice.

2.3 Ocean Data

The Ocean and sea-ice ReAnalyses System 5 (ORAS5) (Zuo et al., 2019) is a reconstruction of ocean and sea-ice states derived from an ocean-sea-ice coupled model driven by atmospheric surface forcing and constrained by ocean observations using data assimilation (Balmaseda et al., 2015). It consists of a behind-real-time component of the OCEAN5 ocean reanalysis-analysis system at ECMWF. The ocean model and data assimilation method are kept frozen during the production of the reanalysis. The Ocean ReAnalysis Pilot system-6 (ORAP6) is a new ocean and

sea-ice reanalysis system that has been developed based on the ECMWF operational OCEAN5 system (Zuo et al., 2021). Despite sharing the same model configurations as OCEAN5, ORAP6 uses updated atmospheric forcing (based on ERA5) and is produced with the most up-to-date reprocessed observation datasets. The ORAP6 data assimilation system has been updated to include a new flow-dependent SST nudging scheme, and to assimilate L3 sea-ice concentration data, among others. ORAP6 uses 3DVar to assimilate in-situ temperature and salinity profiles from Argo, Moorings, XBTs, shipboard CTDs, gliders, and marine mammals, satellite sea-level anomaly and sea-ice concentration data, as well as SST and sea-surface salinity (SSS) nudging in the surface (Zuo et al., 2021). Two sets of ocean data from ORAP6 system have been used in this study. ORAP6.1 is the first version of ORAP6 reanalysis that includes assimilation of all observations. We also consider a control version of ORAP6.1 called "ORAP6-ctrl", which uses the same model setup and atmospheric forcing (from ERA5) as ORAP6.1, but only uses SST and SSS nudging at the surface. The difference between ORAP6.1 and ORAP6-ctrl thus indicates the impact of data assimilation on ocean heating rates.

In addition to the above ocean reanalyses, we determine ocean heating rates from two Argo-based datasets. The first is an Argo-only time series obtained from the combination of a 10/2021 update of the Roemmich and Gilson (2009) climatology and the Asia-Pacific Data-Research Center's Argo gridded 3°x3° monthly product on standard depth levels, documented online (at http://apdrc.soest.hawaii.edu/projects/Argo/index.php). The second Argo-based dataset is an updated version of the 0–2,000 m ocean heat uptake estimate used in Loeb et al. (2021), which is based upon Argo in-situ and satellite altimetry data. It uses local correlations between sea-surface height and ocean heat content anomalies to employ satellite altimetry data as a first guess at ocean heat content where (or when) in situ temperature data are sparse (Willis et al., 2003).

3.0 Methodology

3.1 Inferred Surface Total and Turbulent Heat Fluxes

The surface energy flux (F_S) defined here as positive downwards is inferred using the residual method from the atmospheric energy budget (Trenberth and Fasullo, 2017; Mayer et al., 2017; Liu et al., 2020) as follows:

$$F_S = F_{TOA} - \nabla \cdot F_A - AET \quad (1)$$

where F_{TOA} is the net downward radiation at the TOA, $\nabla \cdot F_A$ is the divergence of lateral atmospheric energy transports (TEDIV), and AET is the vertically integrated atmospheric energy tendency. We use CERES EBAF Ed4.1 to determine F_{TOA}. The $\nabla \cdot F_A$ term is computed from hourly ERA5 analyses of atmospheric wind, temperature, and humidity profiles using an improved budget formulation that treats lateral and vertical moisture enthalpy fluxes in a consistent manner (Mayer et al., 2017) and ensures mass consistency following J. Mayer et al. (2021). Maps of $\nabla \cdot F_A$ are smoothed using a tapered filter truncating at T42. The AET term is calculated from differences of analyses of the total atmospheric energy at the first of each month, but AET is small on the time scales considered.

In addition to the estimates described above, availability of ERA5 short-term forecasts and IFS AMIP data provides two additional estimates of F_{TOA} and F_S and two alternative estimates of $\nabla \cdot F_A$. For ERA5, we use short term forecasts and subtract F_{TOA} and F_S (Eq 1). Neglecting the effect of assimilation increments in this estimate will lead to differences with the divergence estimate based on analysed state quantities (J. Mayer et al 2021). The short-term ERA5 forecasts are initialized from analyses that are constrained by observations and in that sense are still influenced by observations. The divergence estimate from short-term forecasts can thus be viewed as falling somewhere between an analysis-based estimate and an estimate from a free-running

model. The difference between divergence trends estimated from analyses and short-term forecasts provides insight into the degree to which the model can represent observed changes in the atmosphere. It may also reveal areas where the model damps out potential spurious jumps from changes in the observing system. The third divergence estimate is similar to the one based on short-term forecasts but uses IFS AMIP data. Trends in that estimate reflect changes the model captures due to changes in the boundary conditions like SSTs and sea ice.

We determine "inferred" surface turbulent heat fluxes from:

$$Q_S = H_L + H_S = F_S - R_S \tag{2}$$

where Q_S is the sum of surface latent (H_L) and sensible (H_S) heat flux and R_S is net downward radiation at the surface. We determine R_S from CERES.

3.2 Trends

Trends are determined from deseasonalized monthly anomalies using least squares linear regression. To determine trend uncertainties, we first calculate residuals of the linear regression fit to a monthly anomaly time series. Next, we calculate the autocorrelation function (ACF) of the residuals and assess whether or not the ACF at any lag is significant by comparing it with confidence intervals given by:

$$CI_k = \pm t_\alpha \sigma_k \tag{3}$$

where t_α is the student-t statistic at significance level α and σ_k is the standard deviation at lag k derived using the formulation in Mélard and Roy (1987):

$$\sigma_k^2 = \frac{1}{N}\left(1 + 2\sum_{i=1}^{k-1} \rho_i^2\right) \tag{4}$$

where N is the number of samples and ρ_i is the ACF at lag i. If ρ_i at any lag lies outside the confidence intervals in Eq. (3), we account for autocorrelation in determining the trend uncertainty by calculating the effective sample size following Gelman et al. (2013):

$$N_e = \frac{N}{1+2\sum_{i=1}^{m}\rho_i} \quad (5)$$

We determine m as the first lag satisfying both $\rho_{m+1} < 0$ and $\rho_{m+1} + \rho_{m+2} < 0$. This criterion minimizes uncertainty associated with sampling noise in the ACF. If none of the ρ_i fall outside the confidence intervals, we assume the effective sample size (N_e) is equal to *N*. Once N_e is known, Eqs. 3-5 in Santer et al. (2000) are used to calculate the trend uncertainty. While trend uncertainties are evaluated using 2.5–97.5% confidence intervals, we set α=0.8 in Eq. (3) (corresponding to 10-90% confidence intervals) in order to use a less stringent test for autocorrelation in the data. In practice, we generally find statistically significant autocorrelation for monthly data but that is not always the case when using annual mean data with a short 20-year record.

4.0 Results

4.1 Top-of-Atmosphere

Regional trends in TOA net radiation for 03/2000-02/2020 show marked differences between CERES, ERA5 and IFS AMIP (Figs. 1a-c). As noted in prior studies (Myers et al., 2018; Loeb et al., 2018b, 2020), CERES shows pronounced positive trends in net TOA flux over the Eastern Pacific Ocean off of North America. This increase is driven mainly by an ASR increase associated with a reduction in low cloud cover, which in turn is due to increasing SSTs (Myers et al., 2018; Loeb et al., 2018b; Mayer et al., 2018). In contrast, ERA5 shows negative net TOA flux trends throughout most of the Eastern Pacific Ocean region (Fig. 1b), while IFS AMIP shows weaker positive trends and stronger positive trends along the equator (Fig. 1c). That neither ERA5 nor IFS AMIP capture the large positive trend off the west coast of North America observed by CERES may suggest that the low cloud response to SST change is too weak in ERA5 and IFS AMIP. In a similar comparison between CERES and seven CMIP6 models run in AMIP mode (Loeb et al., 2020), most of the models showed increases in net TOA flux in this region but the

magnitude of the change varied amongst the models. Over the Arctic, CERES shows weak trends in net TOA flux—the result of a cancellation between larger trends in ASR and outgoing longwave radiation (not shown). Net TOA flux trends over the Arctic from IFS AMIP are closer to CERES than ERA5, which shows strong negative trends. All three products show positive net TOA flux trends along the climatological Arctic sea ice edge, where the net radiative effect of the retreating sea ice is visible as noted in Hartmann and Ceppi (2014). ERA5 and IFS AMIP show better agreement with CERES over the Atlantic off the coast of North America, to the southwest of Spain and in the west-east trend dipole in the Indian Ocean around 20°-30°S. There is also very good agreement over the sea ice regions off the coast of Antarctica.

Average southern hemisphere (SH) and northern hemisphere (NH) TOA fluxes from CERES for 03/2000-02/2020 show hemispheric symmetry in ASR, stronger LW cooling in the NH, and a larger net heat uptake in the SH (Table 1). The hemispheric asymmetry in net TOA flux requires a 0.17 PW SH-to-NH cross-equatorial heat transport by the ocean-atmosphere system for energy budget closure (Donohoe et al., 2013; Frierson et al., 20013; Marshall et al., 2013; Loeb et al., 2016; Liu et al., 2020). With the exception of NH ASR, the ERA5 ASR and −OLR values in Table 1 fall within the 95% uncertainty of CERES (Loeb et al., 2018a). However, ERA5 mean net fluxes are about half as large as CERES in the SH and more than nine times larger in the NH, while the global mean difference is only 0.05 Wm^{-2}. The ERA5 hemispheric asymmetry in mean net TOA flux implies a −0.006 PW SH-to-NH cross-equatorial heat transport by the ocean-atmosphere system, which is in marked contrast to CERES. For IFS AMIP, the discrepancy with CERES is even greater as the hemispheric contrast in net TOA flux implies a −0.22 PW SH-to-NH cross-equatorial heat transport, and the global mean net flux is negative, both of which are unrealistic. The latter is related to model inconsistencies in the version of the IFS used (see Roberts et al.

2018). A possible reason for the inconsistent hemispheric values could be due to an unrealistic representation of how clouds are distributed between the hemispheres in ERA5 and IFS AMIP. Stephens et al. (2015) showed that increased reflection by clouds in the SH offsets greater reflection by the larger land mass in the NH, resulting in hemispheric symmetry in albedo.

Anomaly standard deviations and trends in ASR, −OLR and NET are fairly symmetric between the hemispheres for CERES (Table 1). The hemispheric trends in CERES between SH and NH differ by only 0.07 Wm^{-2} per decade for ASR, 0.01 Wm^{-2} per decade for −OLR, and 0.08 Wm^{-2} per decade for NET, implying an insignificant 0.02±0.1 PW change to the combined ocean-atmosphere cross-equatorial heat transport over the past 20 years. We note that this does not preclude the possibility of strong but opposing trends in atmospheric and oceanic transport. In contrast to CERES, none of the ERA5 hemispheric and global mean trends in TOA radiation are significant at the 95% level (Table 1). Monthly anomaly standard deviations from ERA5 differ by −22% to −7% relative to CERES. Accordingly, ERA5 monthly anomalies track CERES (Fig. S1), but systematic differences are apparent in ASR and −OLR prior to 2003, and in ASR and NET after 2012. Systematic differences between ERA5 and IFS AMIP for ASR and NET are also apparent after 2012 (Fig. S2). This is likely due to changes in the input data stream in ERA5. After removing the trends in the hemispheric and global monthly mean anomaly time series, the correlation coefficient between ERA5 and CERES is 0.80 for ASR and 0.9 for −OLR and NET. Anomaly standard deviations for IFS AMIP are weaker than ERA5 Forecasts and CERES, but trends are in better agreement with CERES, albeit much smaller in magnitude.

To examine the robustness of the CERES trends, we compare SH, NH and global trends between CERES instruments flying aboard the Terra and Aqua satellites (Fig. 2). The CERES data products in this comparison are the SSF1deg-Terra and SSF1deg-Aqua products, which are used

as input to CERES EBAF (Loeb et al., 2018a). Importantly, in-orbit calibration adjustments with time for CERES instruments on Terra and Aqua are entirely independent of one another. The CERES Terra net TOA flux trends as a function of record length from 03/2000 onwards for SH, NH and global (Figs. 2a-c) show large fluctuations for record lengths shorter than ten years due to internal variability, but patterns of change remain fairly stable for longer record lengths. Global and NH trends exceed the 95% significance level for record lengths greater than 12 years, while it takes 17 years in the SH. Trend differences between Terra and Aqua are smaller than 0.05 Wm^{-2} per decade and fall within the 95% significance level for 07/2002-02/2020 (Figs. 2d-f). The Terra ASR trends (Figs. S3a-c) decrease rapidly with record length early in the record but begin to increase after the record length reaches 14 years, which corresponds to when the Pacific Decadal Oscillation shifted from negative to positive (Loeb et al., 2021). ASR trends from Terra and Aqua are within 0.04 Wm^{-2} per decade of one another for the full period, and remain below the 95% significance level for most shorter record lengths (Figs. S3d-f). Similarly, –OLR trends from Terra and Aqua differ by 0.06 Wm^{-2} per decade of one another, which is also within the 95% significance level (Figs. S4d-f).

Further validation of the CERES record is provided in Loeb et al. (2021), who compared CERES EBAF variations in global mean net TOA flux with estimates of planetary heat uptake from in situ data for mid-2005 to mid-2019. The in situ data used is derived by an inventory of the rates of changes of energy stored in all components of the climate system, with the primary contribution from differences of overlapping annual 0–2,000 m ocean heat content anomalies from Argo float profiles. As shown in Loeb et al. (2021), the trend in the difference between the CERES and in situ data is 0.068±0.29 W m^{-2} $decade^{-1}$, which is similar in magnitude to the comparison between CERES Terra and Aqua. Independent analyses of the CERES data by Stephens et al.

(2022) and Datseris and Stevens (2021) confirm our findings. Additionally, Hakuba et al. (2021) use a combination of altimetric and gravimetric observations from GRACE to find a similar trend in EEI. These results stand in marked contrast with Matthews (2021), who claim that there are "spurious calibration drifts" in the CERES record based upon an analysis of lunar reflectance measured by CERES. A direct comparison between the adjusted CERES Terra reflected SW values proposed by Matthews (2021) and the official CERES SSF1deg Ed4.1 product reveals that Matthews (2021) made the largest "corrections" to the CERES record (reaching –0.8 Wm^{-2}) prior to when CERES Terra even started making lunar observations in 10/2002 (Fig. S5a). If we restrict the comparison only to dates when CERES scans of the moon exist (Fig. S5b), there is virtually no trend difference between the two records (trend difference of –0.012 Wm^{-2} per decade). The CERES lunar data thus confirms that CERES onboard calibration sources are performing nominally.

4.2 Within-Atmosphere Transport

Trends in TEDIV for 2000/03-2020/02 from ERA5 Analysis, ERA5 Forecasts and IFS AMIP are provided in Figs. 3a-c. Regions with positive TEDIV trends correspond to increasingly divergent lateral energy fluxes, and negative trends correspond to convergent fluxes. The trends based on ERA5 forecasts and IFS-AMIP are similar to those from ERA5 Analysis over ocean, suggesting that the ERA5 Analysis patterns are not a spurious signal from changes in the observing system. All three results show that the magnitudes of TEDIV trends generally exceed those for net TOA flux (Figs. 1a-c). Large positive trends in TEDIV are observed over the eastern Pacific Ocean to the north and south of the Intertropical Convergence Zone (ITCZ), where trends are weakly negative but intensify towards the west over the Maritime Continent. Trends over the Indian Ocean and North Atlantic are generally negative, except over the Gulf Stream, where a strong positive

trend is apparent in all three results. Except for the area of positive TEDIV trends stretching from the Barents and Kara Seas, trends over the Arctic Ocean are generally negative, but the magnitude of the trends differs between these three results, with ERA5 forecasts showing the strongest negative trends. Over the Barents and Kara Seas, the increase in divergence is likely due to sea ice loss, which leads to enhanced surface-to-atmosphere heat flux and divergence of energy.

Over land, trends for ERA5 analysis are notably greater in magnitude compared to both ERA5 forecast and IFS-AMIP. This points to a greater uncertainty associated with TEDIV derived directly from atmospheric profiles over land. Before computing TEDIV, we perform a vertically uniform correction to the winds to achieve mass conservation. As such, there is no correction for errors in the vertical structure of the wind divergence (as the vertical error structure is hard to estimate), which over topography are likely larger (also arising from numerical noise). TEDIV also contains vertical covariances between atmospheric energy and wind divergence (i.e., the vertical error structure of the wind divergence will project on TEDIV). Since the wind divergence errors likely have trends as well (e.g. from changes in the observing system), we see noisy trend patterns in TEDIV over land. While a substantial fraction of the noisy patterns seen from the ERA5 fields is related to numerical noise over topography, some of the non-zero trends over land are similar in ERA5 analysis and ERA5 forecasts (e.g. over central Africa), which suggests spurious jumps in the observing system in that area affecting both analyses and short-term forecasts. Some of the features of TEDIV trends over land may also be realistic and balance observed trends in net TOA flux, such as the negative trends over northern China (compare Figs 3b and 1a).

Despite large regional trends in TEDIV, hemispheric average trends are near zero for ERA5 Analysis (Table 2). Global TEDIV trends based on analyses should be exactly zero. This is not the case for ERA5 forecasts since the effect of assimilation increments are not included. Global

trends in IFS-AMIP TEDIV should also be close to zero since the model conserves energy (to a relatively high degree).

4.3 Surface

Trend maps of F_S using the Inferred method (Eq. 1), ERA5 forecasts and IFS AMIP are provided in Figs. 4a-c. In the latter two cases, F_S is determined from the sum of R_S, H_L, and H_S. Comparing Figs. 3a and 4a, it is evident that regional trend patterns and magnitudes in F_S are mainly determined by those in TEDIV. This is consistent with what previous studies have shown for spatial patterns in climatological mean F_S (Liu et al. 2020; Mayer et al. 2017; Trenberth and Fasullo 2017). As a consequence, trends for the Inferred method over land are largely spurious (see Section 4.2).

Over ocean, large-scale patterns of surface flux trends from the three methods are similar over the Southern Ocean, Southern Indian Ocean, Barents Sea, and the Kuroshio Current and Gulf stream. Trends over the Gulf Stream are particularly noteworthy, as all three results show large negative trends, implying increased surface-to-atmosphere heat flux. In this region, the climatological mean F_S is also strongly negative since the atmosphere is supplied energy from warm water masses transporting energy poleward (Trenberth and Fasullo, 2017; Mayer et al., 2021). We also find large negative trends for Inferred (Fig. 4a) and ERA5 forecasts (Fig. 4b) over the East Pacific off of North and South America and a line of positive trends along the equatorial Pacific stretching from the Maritime Continent to Central America. All three products show significant positive trends in the Atlantic between the equator and ~40N. The trends are generally more pronounced for Inferred than for ERA5 Forecasts. In contrast, this trend pattern is less evident for IFS AMIP (Fig. 4c), which entirely misses the positive trends along the equator.

In order to further decompose trends in F_S in terms of radiative and non-radiative components, we compute trends in net total radiative flux at the surface (R_S) from CERES (Fig. 5a) and determine the "inferred" surface turbulent flux (Q_S) trends based upon Eq. (2) in Fig. 6a. These are compared with regional trends in R_S and Q_S for ERA5 Forecasts (Figs. 5b and 6b). In Fig. 6b, Q_S is obtained directly from the sum of H_L and H_S. While the trend patterns in R_S are similar between CERES and ERA5 Forecasts, their magnitudes are quite different. Large differences are evident over the west tropical Pacific Ocean, where ERA5 Forecasts shows large positive trends that are absent in CERES. Regional trend patterns in Q_S are similar over ocean, but the inferred method produces generally larger values. There is good agreement over the eastern Pacific off the west coast of the Americas, where trends are predominantly negative. Trends in Q_S are generally much larger than those in R_S, suggesting a dominant role for surface turbulent heat flux over net surface radiation at regional scales.

Trends in surface turbulent flux from the SeaFlux V3 (Roberts et al., 2020) and OAFlux V3 (Yu and Weller, 2007) products for 08/2002-07/2018 (Figs. S6a-b) are generally in poor agreement everywhere. The lack of agreement is surprising since SeaFlux and OAFlux are dedicated surface turbulent heat products. According to Robertson et al. (2020), trends from these products are less reliable due to problems with wind speed retrievals from Special Sensor Microwave Imager/Sounder satellite sensors and excessive upward trends in Optimal Interpolation Sea Surface Temperature (OISST) data.

4.4 Within Ocean

A benefit of ocean reanalysis is that it provides continuous coverage of the global oceans and therefore can resolve higher frequency variability of ocean heating rate than methods that rely primarily on in situ data like Argo. We compare ORAS5, ORAS6.1 and ORAS6-ctrl global

monthly anomalies in full-depth global ocean heating rate for 03/2000-02/2020 (Figs. 7a-c) and the hemispheric and global averages, anomaly standard deviations and trends (Table 3). Anomalies for ORAS5 and ORAP6.1 are similar and show a correlation of 0.5. In contrast, ORAP6-ctrl shows much weaker variability than the other two reanalyses, with a monthly standard deviation that is 38% smaller than ORAP6.1, and a correlation with ORAP6.1 of only 0.31. This implies that assimilating more data significantly increases higher-frequency variability. ORAP6.1 shows a sudden decrease around 2005 (Fig. 7b) that is not apparent in ORAS5 or ORAP6.1-ctrl. This dip causes the trend in ORAP6.1 for 07/2005-12/2019 (Table 4) to be much larger than for 03/2000-02/2020 (Table 3). The dip in ORAP6.1 is likely caused by the model bias correction method. Prior to 2005, ORAP6.1 heating rates are similar to ORAS5 but ocean temperatures are much warmer than ORAS5 in the Southern Ocean. When Argo data are assimilated, the ORAP6.1 data assimilation increment cools the ocean, causing a sudden decrease in ocean heating rate around 2005. This problem illustrates one of the greatest challenges in ocean reanalyses: how to balance the temporal consistency of the model simulation with the increased accuracy of the state estimation in the data rich periods. This underscores the need for improved treatments of model error in reanalyses.

Agreement among global annual variations in CERES net TOA flux and ocean heating rate for the three ocean reanalyses, Argo-only, and combined Argo and satellite altimetry data (Argo+SA) is mixed (Figs. 8a-e). Of the three reanalyses (Figs. 8a-c), ORAP6-ctrl provides the best agreement with CERES prior to 2013. After 2013, ORAP6-ctrl ocean heating rates are smaller than those for ORAS5 and ORAP6.1, which show better agreement with CERES for that period. This suggests that surface forcing and SST information alone are sufficient to estimate ocean heating rate variability during some periods, but in other periods subsurface information may be

necessary. When only Argo data are considered, annual variations are very noisy (Fig. 8d). The variability is much greater for 0-2000 m than 0-700 m, a finding also noted in Trenberth et al. (2016). The noise is significantly reduced when Argo and satellite altimetry data are combined (Fig. 8e). Nevertheless, the Argo-only and Argo+SA global trends are similar to CERES while ORAP5 and ORAP6-ctrl show weaker trends (Tables 1 and 4). As noted earlier, ORAP6.1 trends are much larger due to the discontinuity around 2005.

With the exception of ORAP6.1, all of the datasets show larger hemispheric mean ocean heating rates for the SH than the NH for 07/2005-12/2019 (Table 4). Overall, ORAS6-ctrl shows the best agreement with Argo and Argo+SA. For ORAP6.1, the SH heating rate is a factor of 2.5 smaller than the NH value, and a factor of 3 smaller compared to the SH values from the other datasets in Table 4.

A general consensus amongst all of the ocean datasets is a tendency for larger trends in ocean heating rate in the NH than the SH after 2005 (Table 4), but there is poor agreement on the magnitude of the trends. This makes determination of trends in ocean heat transport derived as a residual between net surface flux and ocean heating rate highly uncertain.

5. Summary

This study uses satellite and atmospheric and oceanic reanalysis datasets to address the following question: *To what extent can we trust observed 20-year trends in different components of Earth's energy budget and energy flows within the climate system".* We focus on trends after 2000 in TOA radiation, TEDIV, surface flux, and within-ocean heating rate using satellite observations from CERES and different versions of atmospheric and oceanic reanalysis datasets from ECMWF. As the trends are likely influenced by both anthropogenic forcing and internal variability, there is no expectation that these are solely representative of longer term trends.

Regional trends in TOA net downward radiation from CERES, ERA5 and IFS AMIP are markedly different over the Eastern Pacific Ocean off of North America, where large increases in SST have been observed during the CERES period. Whereas CERES observes large positive trends associated with a reduction in low cloud cover, ERA5 shows negative net TOA flux trends throughout most of the Eastern Pacific Ocean region and IFS AMIP shows weaker positive trends. These results suggest that the low cloud response to SST change may be too weak in ERA5 and IFS AMIP. ERA5 and IFS AMIP show better agreement with CERES over the Atlantic off of North America and Europe, the Indian Ocean between 20°-30°S, and over sea ice regions off the coast of Antarctica. Trends are generally inconsistent over the Arctic Ocean, except in areas near the sea ice edge that are associated with steep declines in sea ice concentration. We find that CERES global mean trends appear to be robust based upon multiple lines of evidence, including direct comparisons between CERES instruments on Terra and Aqua (consistent to < 0.1 W m^{-2} $decade^{-1}$), comparisons with in-situ measurements from Argo and results that use a combination of altimetric and gravimetric observations from GRACE.

CERES trends in net TOA flux between the SH and NH are very close to one another, implying an insignificant 0.02±0.1 PW change to the combined ocean-atmosphere cross-equatorial heat transport over the first 20 years of the 21st century. ERA5 and IFS AMIP also show insignificant hemispheric trend differences, but their SH, NH and global mean trends are smaller than CERES. Surprisingly, ERA5 climatological average net TOA fluxes are approximately half as large as CERES in the SH and more than nine times larger in the NH, while the global mean difference is only 0.05 Wm^{-2}. The ERA5 and IFS AMIP hemispheric asymmetries in mean net TOA flux imply a NH-to-SH cross-equatorial heat transport by the ocean-atmosphere system. That is in marked contrast to CERES, which shows a 0.17 PW SH-to-NH cross-equatorial heat

transport, consistent with expectation (Frierson et al., 2013). A possible reason for the inconsistent hemispheric values in ERA5 and IFS AMIP could be due to an unrealistic representation of how clouds are distributed between the hemispheres.

We compare TEDIV calculated directly from ERA5 analysed profiles of temperature, humidity and winds (ERA5 Analysis) with TEDIV obtained as a residual between TOA and surface fluxes from ERA5 short-term forecasts and IFS AMIP. Trends based on ERA5 forecasts and IFS AMIP are similar to those from ERA5 Analysis over ocean, suggesting that the ERA5 Analysis patterns are not a spurious signal from changes in the observing system. Regional trends in F_S are determined mainly by those in TEDIV, and therefore exhibit similar features. We find consistent negative trends over the Gulf Stream, implying increased surface-to-atmosphere heat flux. Increases surface-to-atmosphere heat flux are also observed over large portions of the eastern Pacific Ocean off the coasts of North and South America. While trend patterns in net surface radiation are similar between CERES and ERA5 Forecasts, large differences are evident over the west tropical Pacific Ocean, where ERA5 Forecasts show large positive trends not observed by CERES. Regional trends in surface turbulent heat flux from an inferred method that uses an energy budget constraint involving CERES and ERA5 analysis data show a similar pattern over ocean to that obtained from the direct sum of sensible and latent heat from ERA5 Forecasts. In contrast, trends from SeaFlux V3 and OAFlux V3 show poor agreement likely because of an excessive trend in OISST input data.

Comparisons of monthly ocean heating rates amongst ORAS5, ORAP6.1 and ORAP6-ctrl illustrate some of the challenges associated with ocean reanalysis. The ORAP6-ctrl is a control version of ORAP6.1 that uses the same model setup and atmospheric forcing as ORAP6.1, but only uses SST and SSS nudging at the surface. The difference between ORAP6.1 and ORAP6-ctrl

556 thus indicates the impact of data assimilation on ocean heating rates. While anomalies for ORAS5
557 and ORAP6.1 are similar, variability for ORAP6-ctrl is 38% weaker than ORAP6.1. This implies
558 that assimilating more data significantly increases higher-frequency variability. ORAP6.1 also
559 shows a sudden decrease around 2005 that is not apparent in ORAS5 or ORAP6.1-ctrl, which
560 causes a spurious trend in ORAP6.1. This dip is likely associated with a warm bias in the model
561 that gets corrected after the introduction of Argo data in 2005 by the data assimilation increment,
562 leading to a steep decline in ocean heating rate. Balancing the temporal consistency between the
563 model simulation and introduction of new data in a time series remains a challenge in both ocean
564 and atmosphere reanalysis systems. The impact on trends can be especially large, depending on
565 the magnitude of the model bias and the location within the time series new data are
566 introduced/removed.

567 Global annual variations in CERES net TOA flux and ocean heating rate for the three ocean
568 reanalyses, Argo-only, and combined Argo and satellite altimetry data (Argo+SA) are also
569 compared. Of the three reanalyses, ORAP6-ctrl provides the best agreement with CERES up to
570 2013, while ORAS5 and ORAP6.1 are in better agreement with CERES after 2013. From this we
571 conclude that surface forcing and SST information may be sufficient to estimate ocean heating rate
572 variability for some periods, but other periods may also require subsurface information.

573 All of the ocean datasets except ORAP6.1 show larger hemispheric mean ocean heating
574 rates for the SH than the NH. ORAS6-ctrl shows the best overall agreement with Argo and
575 Argo+SA. For ORAP6.1, the SH heating rate is a factor of 2.5 smaller than the NH value, and a
576 factor of 3 smaller compared to the SH values from the other datasets. All of the ocean datasets
577 show larger trends in ocean heating rate in the NH than the SH after 2005, but there is poor

agreement on the magnitude of the trends. Consequently, determination of trends in ocean heat transport derived as a residual between net surface flux and ocean heating rate is highly uncertain.

Acknowledgements

We thank the CERES science, algorithm, and data management teams and the NASA Science Mission Directorate for supporting this research. CERES_EBAF Ed4.1 was obtained from the CERES ordering page at http://ceres.larc.nasa.gov/order_data.php. ERA5 data are publicly available via the Copernicus Climate Change Service climate. (https://confluence.ecmwf.int/display/CKB/). MM's contribution was funded by EU H2020 Grant agreement No. 862626 (EUROSEA) as well as Austrian Science Fund project P33177. This is PMEL Contribution Number 5351.

6. Figure Captions

Figure 1. Trends in TOA Net Radiation for 2000/03-2020/02. (a) CERES-EBAF, (b) ERA5 forecasts and (c) IFS AMIP.

Figure 2. CERES net TOA flux trends against record length for CERES SSF1deg Terra (top) and Terra – Aqua (bottom) for (a, d) SH, (b, e) NH, (c, f) Global. Start date is 03/2000 for Terra and 07/2002 for Terra – Aqua. Gray shading corresponds to 95% confidence interval.

Figure 3. Trends in TEDIV for 2000/03-2020/02. (a) ERA5 Analysis (directly from wind, T, q etc), (b) ERA5 forecasts (net TOA – FS) and (c) IFS AMIP (net TOA – FS).

Figure 4. Trends in surface flux (positive downward) for 2000/03-2020/02. (a) Inferred (CERES TOA Net − ERA5 TEDIV), (b) ERA5 forecasts and (c) IFS AMIP.

Figure 5. Trend for 200208-202002 in net total radiative flux at the surface (positive down) from (a) CERES and (b) ERA5 forecasts.

Figure 6. Trends in surface turbulent heat flux (positive downward) for 2002/08-2020/02. (a) Inferred (CERES TOA Net − ERA5 TEDIV − CERES Surface Net) and (b) ERA5 forecasts.

Figure 7. Monthly global anomalies in ocean heating rate for (a) ORAS5, (b) ORAP6.1, (c) ORAP6-ctrl.

Figure 8. Global annual mean variation in CERES net TOA flux and ocean heating rate for 0-700 m and full-depth or 0-2000 m for: (a) ORAS5; (b) ORAP6.1; (c) ORAP6-ctrl; (d) Argo; (e) Argo+SLA.

7. References

Bryan, K. 1982. Poleward heat transport by the ocean: Observations and models. *Ann. Rev. Earth Planet. Sci. 10,* 15-30.

Buizza, R., and Coauthors, 2018: Advancing global and regional reanalyses. Bull. Amer. Meteor. Soc., 99, ES139–ES144, https://doi.org/10.1175/BAMS-D-17-0312.1.

Collins, W. D., P. J. Rasch, B. E. Eaton, B. V. Khattatov, J.-F. Lamarque, and C. S. Zender, 2001: Simulating aerosols using a chemical transport model with assimilation of satellite aerosol retrievals: Methodology for INDOEX. J. Geophys. Res., 106, 7313–7336, doi:10.1029/2000JD900507.

Datseris, G., & Stevens, B. (2021). Earth's albedo and its symmetry. AGU Advances, 2, e2021AV000440. https:// doi.org/10.1029/2021AV000440.

Dee, D. P., M. Balmaseda, G. Balsamo, R. Engelen, A. J. Simmons, and J.-N. Thépaut, 2014: Toward a consistent reanalysis of the climate system. Bull. Amer. Meteor. Soc., 95, 1235–1248, https://doi.org/10.1175/BAMS-D-13-00043.1.

Dines, W. H., 1917: The heat balance of the atmosphere, J. R. Meteorol. Joc., 43, 151-158.

Doelling, D. R., and Coauthors, 2013: Geostationary enhanced temporal interpolation for CERES flux products. J. Atmos. Oceanic Technol., 30, 1072–1090, https://doi.org/10.1175/JTECH-D-12-00136.1.

Donohoe A., J. Marshall, D. Ferreira, D. McGee, 2013: The relationship between ITCZ location and atmospheric heat transport across the equator: from the seasonal cycle to the last glacial maximum. J. Climat, 26:3597–3618. doi:10.1175/JCLI-D-12-00467.1.

Fasullo, J. T., and K. E. Trenberth, 2008a: The annual cycle of the energy budget: Part I: Global mean and land–ocean exchanges. J. Climate, 21, 2297–2312, https://doi.org/10.1175/2007JCLI1935.1.

Fasullo, J. T., and K. E. Trenberth, 2008b: The annual cycle of the energy budget: Part II: Meridional structures and poleward transports. J. Climate, 21, 2313–2325, https://doi.org/10.1175/2007JCLI1936.1.

Frierson, D. M. W., Y.-T. Hwang, N. S. Fuckar, R. Seager, S. M. Kang, A. Donohoe, E. A. Maroon, X. Liu, D. S. Battisi, 2013: Contribution of ocean overturning circulation to tropical rainfall peak in the northern hemisphere. Nat Geosci. doi:10.1038/NGEO1987.

Gelaro, R., and Coauthors, 2017: The Modern-Era Retrospective Analysis for Research and Applications, Version 2 (MERRA-2), J. Climate, 30, 5419-5454. DOI: 10.1175/JCLI-D-16-0758.1.

Gelman, A., J. B. Carlin, H. S. Stern, D. B. Dunson, A. Vehtari, and D. B. Rubin, 2013: Bayesian Data Analysis. Third Edition. London: Chapman & Hall / CRC Press. 654 pp.

Hakuba, M. Z., Frederikse, T., & Landerer, F. W. (2021). Earth's energy imbalance from the ocean perspective (2005–2019). Geophysical Research Letters, 48, e2021GL093624. https://doi.org/10.1029/2021GL093624.

Hartmann, Dennis L. and Paulo Ceppi, 2014: Trends in the CERES Data Set 2000-2013: The Effects of Ice Melt and Jet Shifts and Comparison to Climate Models. *J. Climate* , 27, doi:10.1175/JCLI-D-13-00411.1, 2444-2456

Hersbach, H., and Coauthors, 2020:TheERA5global reanalysis.Quart. J. Roy. Meteor. Soc., 146, 1999–2049, https://doi.org/10.1002/qj.3803.

Hersbach, H., C. Peubey, A. J. Simmons, P. Berrisford, P. Poli, and D. P. Dee, 2015: ERA-20CM: a twentieth-century atmospheric model ensemble. Quarterly Journal of the Royal Meteorological Society, 141, 2350–2375.

Hunt, G. E., R. Kandel, and A. T. Mecherikunnel, 1986: A history of presatellite investigations of Earth's radiation budget. Rev. Geophys., 24, 351-356.

Johnson, G. C., Hosoda, S., Jayne, S. R., Oke, P. R., Riser, S. C., Roemmich, D., ... & Xu, J. (2022). Argo—Two Decades: Global Oceanography, Revolutionized. Annual review of marine science, 14, 379-403.

Kato, S., N. G. Loeb, J. T. Fasullo, K. E. Trenberth, P. H. Lauritzen, F. G. Rose, D. A. Rutan, and M. Satoh, 2021: Regional energy and water budget of a precipitating atmosphere over ocean. J. Climate, 34, DOI: 10.1175/JCLI-D-20-0175.1.

Kato, S., F. G. Rose, D. A. Rutan, T. J. Thorsen, N. G. Loeb, D. R. Doelling, X. Huang, W. L. Smith, W. Su, and S.-H. Ham, 2018: Surface irradiances of Edition 4.0 Clouds and the Earth's Radiant Energy System (CERES) Energy Balanced and Filled (EBAF) data product. J. Climate, 31, 4501-4527. DOI: 10.1175/JCLI-D-17-0523.1.

Kato, S., N. G. Loeb, J. T. Fasullo, K. E. Trenberth, P. H. Laurizen, F. G. Rose, D. A. Rutan, and M. Satoh, 2021: Regional energy and water budget of a precipitating atmosphere over ocean. J. Climate (in press).

L'Ecuyer, T. S., H. Beaudoing, M. Rodell, W. Olson, B. Lin, S. Kato, C. A. Clayson, E. Wood, E. Clark, R. Adler, G. Huffman, M. Bosilovich, F. Robertson, J. S. Famiglietti, P. R. Houser, D. Chambers, E. Fetzer, X. Gao, G. Gu, K. Hilburn, D. P. Lettenmaier, W. T. Liu, C. A. Schlosser, and J. Scheffield, 2015: The observed state of global energy balance in the early 21st century. *J. Climate*, **28**, 8319-8346.

Liu, C., R. P. Allan, M. Mayer, R. Hyder, D. Desbruyeres, L. Cheng, J. Xu, F. Xu, and Y. Zhang, 2020: Variability in the global energy budget and transports 1985-2017. Climate Dynamics, 55:3381–3396. https://doi.org/10.1007/s00382-020-05451-8.

Loeb, N. G., D. A. Rutan, S. Kato, and W. Wang, 2014: Observing interannual variations in Hadley circulation atmospheric diabatic heating and circulation strength, *J. Climate*, 27, DOI: 10.1175/JCLI-D-13-00656.1.

Loeb, N.G., H. Wang, A. Cheng, S. Kato, J.T. Fasullo, K.-M. Xu, and R.P. Allan, 2016: Observational constraints on atmospheric and oceanic cross-equatorial heat transports: Revisiting the precipitation asymmetry problem in climate models. Climate Dynamics, 46(9-10), 3239-3257. doi:10.1007/s00382-015-2766-z.

Loeb, N.G., N. Manalo-Smith, W. Su, M. Shankar, and S. Thomas, 2016: CERES top-of-atmosphere Earth radiation budget climate data record: Accounting for in-orbit changes in instrument calibration. *Remote Sens*., 8, 182; doi:10.3390/rs8030182.

Loeb, N. G., Doelling, D. R., Wang, H., Su, W., Nguyen, C., Corbett, J. G., et al. (2018a). Clouds and the Earth's Radiant Energy System (CERES) energy balanced and filled (EBAF) top-of-atmosphere (TOA) Edition 4.0 data product. Journal of Climate, 31, 895–918. https://doi.org/10.1175/JCLI-D-17-0208.1.

Loeb, N.G., T.J. Thorsen, J.R. Norris, H. Wang, and W. Su, 2018b: Changes in Earth's energy budget during and after the "Pause" in Global Warming: An observational perspective. MDPI Climate, 6, 62; doi:10.3390/cli6030062.

Loeb, N. G., H. Wang, R. P. Allan, T. Andrews, K. Armour, J.N.S. Cole, et al., 2020: New generation of climate models track recent unprecedented changes in earth's radiation budget observed by CERES. Geophysical Research Letters, 47, doi:10.1029/2019GL086705.

Loeb, N. G., G. C. Johnson, T. J. Thorsen, J. M. Lyman, F. G. Rose, and S. Kato, 2021: Satellite and ocean data reveal marked increase in Earth's heating rate. Geophys. Res. Lett., 48, e2021GL093047. https://doi.org/10.1029/2021GL093047.

London, J., 1957: A study of the atmospheric heat balance, final report, contract USAF8S1911221165, New York Univ., New York.

Marshall J., A. Donohoe, D. Ferreira, and D. McGee, 2013: The ocean's role in setting the mean position of the inter-tropical convergence zone. Clim Dyn. doi:10.1007/s00382-013-1767-z.

Matthews, G., 2021: NASA CERES spurious calibration drifts corrected by lunar scans to show the Sun is not increasing global warming and allow immediate CRF detection. Geophys. Res. Lett., 48, e2021GL092994. https://doi.org/10.1029/2021GL092994.

Mayer, J., M. Mayer, and L. Haimberger, 2021: Consistency and homogeneity of atmospheric energy, moisture, and mass budgets in ERA5. J. Climate, 34(10), 3955-3974.

Mayer, M., L. Haimberger, J. M. Edwards, and P. Hyder, 2017: Toward consistent diagnostics of the coupled atmosphere and ocean energy budget, J. Climate, 30, DOI: 10.1175/JCLI-D-17-0137.1.

Mayer, M., and L. Haimberger, L., 2012: Poleward atmospheric energy transports and their variability as evaluated from ECMWF reanalysis data. J. of Climate, 25(2), 734–752. https://doi.org/10.1175/JCLI-D-11-00202.1.

Mayer, M., L. Haimberger, and M. A. Balmaseda, 2014: On the energy exchange between tropical ocean basins related to ENSO. *J. Climate*, *27*(17), 6393-6403.

Mayer, M., Alonso Balmaseda, M., & Haimberger, L. (2018). Unprecedented 2015/2016 Indo-Pacific heat transfer speeds up tropical Pacific heat recharge. *Geophysical research letters*, *45*(7), 3274-3284.

Mélard, G., and R. Roy, 1987: On confidence intervals and tests for autocorrelations. Comp. Stat. Data Analysis, 5, 31-44.

Minnis, P., S. Sun-Mack, Y. Chen, F. Chang, C. R. Yost, W. L. Smith, P. W. Heck, R. F. Arduini, S. T. Bedka, Y. Yi, G. Hong, Z. Jin, D. Painemal, R. Palikonda, B. R. Scarino, D. A. Spangenberg, R. A. Smith, Q. Z. Trepte, P. Yang, Y. Xie, 2020: CERES MODIS Cloud Product Retrievals for Edition 4–Part I: Algorithm Changes. IEEE Transactions on Geoscience and Remote Sensing, 1-37. doi: 10.1109/TGRS.2020.3008866.

Myers, T. A., C. R. Mechoso, G. V. Cesana, M. J. DeFlorio, and D. E. Waliser, 2018: Cloud feedback key to marine heatwave off Baja California. Geophysical Research Letters, 45, 4345–4352. https://doi.org/10.1029/2018GL078242.

Oort, A. H., and T. H. Vonder Haar, 1976: On the observed annual cycle in the ocean–atmosphere heat balance over the Northern Hemisphere. J. Phys. Oceanogr., 6, 781–800.

Raghuraman, S. P., D. J. Paynter, and V. Ramaswamy, 2021: Anthropogenic forcing and response yield observed positive trend in Earth's energy imbalance. *Nature Communications*, 12, 4557, DOI:10.1038/s41467-021-24544-4.

Rienecker, M. M., and Coauthors, 2008: The GEOS-5 Data Assimilation System—Documentation of versions 5.0.1, 5.1.0, and 5.2.0. NASA Tech. Memo. NASA/TM-2008-104606, Vol. 27, 97 pp., http://gmao.gsfc.nasa.gov/pubs/docs/Rienecker369.pdf.

Roberts, J. B., C. A. Clayson, and F. R. Robertson, 2020: SeaFlux v3: An updated climate data record of ocean turbulent fluxes. https://doi.org/10.5067/SEAFLUX/DATA101; data available at https://ghrc.nsstc.nasa.gov/pub/SEAFLUX/.

Roberts, C. D., Senan, R., Molteni, F., Boussetta, S., Mayer, M., & Keeley, S. P. (2018). Climate model configurations of the ECMWF Integrated Forecasting System (ECMWF-IFS cycle 43r1) for HighResMIP. *Geoscientific model development*, *11*(9), 3681-3712.

Robertson, F. R., and Coauthors, 2020: Uncertainties in ocean latent heat flux variations over recent decades in satellite-based estimates and reduced observation reanalyses. J. Climate, 33, 8415–8437, https://doi.org/10.1175/JCLI-D-19-0954.1.

Rutan, D., F. Rose, M. Roman, N. Manalo-Smith, C. Schaaf, and T. Charlock, 2009: Development and assessment of broadband surface albedo from Clouds and the Earth's Radiant Energy System clouds and radiation swath data product. J. Geophys. Res., 114, D08125, doi:10.1029/2008JD010669.

Rutan, D. A., S. Kato, D. R. Doelling, F. G. Rose, L. T. Nguyen, T. E. Caldwell, and N. G. Loeb, 2015: CERES synoptic product: Methodology and validation of surface radiant flux. *J. Atmos. Oceanic Technol.*, **32**, 1121–1143, doi: 10.1175/JTECH-D-14-00165.1.

Santer, B. D., T. M. L. Wigley, J. S. Boyle, D. J. Gaffen, J. J. Hnilo, D. Nychka, et al., 2000: Statistical significance of trends and trend differences in layer-average atmospheric temperature time series. J. Geophys. Res., 105, 7337–7356. https://doi.org/10.1029/1999jd901105

Shankar, M., W. Su, N. Manalo-Smith, N. G. Loeb, 2020: Generation of a Seamless Earth Radiation Budget Climate Data Record: A New Methodology for Placing Overlapping Satellite Instruments on the Same Radiometric Scale. Remote Sensing, 12(17), 2787. doi: 10.3390/rs12172787.

Stephens, G. L., M. Z. Hakuba, S. Kato, A. Gettleman, J.-L. Dufresne, T. Andrews, J.N.S. Cole, U. Willem, and T. Mauritsen, 2022: The changing nature of Earth's reflected sunlight. Proc. Royal Soc. (submitted).

Stephens, G. L., J. Li, M. Wild, C. A. Clayson, N. Loeb, S. Kato, T. L'Ecuyer, P. W. Stackhouse, M. Lebsock, and T, Andrews, 2012: An update on Earth's energy balance in light of the latest global observations, *Nature Geoscience*, **5**, DOI: 10.1038/NGEO1580.

Stephens G. L., D. O'Brien, P. J. Webster, P. Pilewski, S. Kato, J.-L. Li, 2015: The albedo of Earth. Rev Geophys. doi:10.1002/2014RG000449.

Storto, A., et al., 2019: Ocean Reanalyses: Recent Advances and Unsolved Challenges. Front. Mar. Sci, 6:418. doi: 10.3389/fmars.2019.00418.

Trenberth, K. E., 1979: Mean annual poleward energy transports by the oceans in the Southern Hemisphere. Dyn. Atmos. Oceans, 4, 57–64.

Trenberth, K. E., and J. M. Caron, 2001: Estimates of meridional atmosphere and ocean heat transports. J. Climate, 14, 3433-3443.

Trenberth, K. E., and J. T. Fasullo, 2008: An observational estimate of inferred ocean energy divergence, J. Phys. Oceanog., 38, DOI: 10.1175/2007JPO3833.1.

Trenberth, K. E., J. T. Fasullo, and J. Kiehl, 2009: Earth's global energy budget, *Bull. Amer. Meteor. Soc.*, DOI: 10.1175/2008BAMS2634.1.

Trenberth, K. E., J. T. Fasullo, and J. Mackaro, 2011: Atmospheric moisture transports from ocean to land and global energy flows in reanalyses. J. Climate, 24, 4907–4924, https://doi.org/10.1175/2011JCLI4171.1.

Trenberth, K. E., J. T. Fasullo, K. von Schuckmann, and L. Cheng, Insights into Earth's energy imbalance from multiple sources. J. Climate, 29, 7495-7505, doi: 10.1175/JCLI-D-16-0339.1.

Trenberth, K. E., and J. Fasullo, 2017: Atlantic meridional heat transports computed from balancing Earth's energy locally. Geophys. Res. Lett., 44, 1919-1927, doi:10.1002/2016GL072475.

Trenberth, K. E., and J. Fasullo, 2018: Applications of an updated atmospheric energetics formulation. *J. Climate*, **31**, 6263-6279, Doi: 10.1175/JCLI-D-17-0838.

Vonder Haar, T. H., and A. H. Oort, 1973: A new estimate of annual poleward energy transport by the oceans. J. Phys. Oceanogr., 3, 169–172.

Wild, M., D. Folini, C. Schär, N. Loeb, N., E. G. Dutton, G. König-Langlo, 2013: The global energy balance from a surface perspective. *Climate Dynamics,* 40, 3107-3134, 2013 https://doi.org/doi:10.1007/s00382-012-1569-8.

Willis, J. K., D. Roemmich, and B. Cornuelle, 2003: Combining altimetric height with broadscale profile data to estimate steric height, heat storage, subsurface temperature, and sea-surface temperature variability. Journal of Geophysical Research, 108. https://doi.org/10.1029/2002jc001755.

Yu, L., 2019: Global air–sea fluxes of heat, fresh water, and Momentum: Energy budget closure and unanswered questions. Annu. Rev. Mar. Sci., 11, 227-248. https://doi.org/10.1146/annurev-marine-010816-060704.

Yu, L., and R. A. Weller, 2007: Objectively analyzed air–sea heat fluxes for the global ice-free oceans (1981–2005). Bull. Amer. Meteor. Soc., 88, 527–540, https://doi.org/10.1175/BAMS-88-4-527.

Zuo, H., M. A. Balmaseda, E. de Boisseson, S. Tietsche, M. Mayer, and P. de Rosnay, 2021: The ORAP6 ocean and sea-ice reanalysis: description and evaluation, EGU General Assembly

2021, online, 19–30 Apr 2021, EGU21-9997, https://doi.org/10.5194/egusphere-egu21-9997, 2021.

Zuo, H., M. A. Balmaseda, S. Tietsche, K. Mogensen, and M. Mayer, 2019:The ECMWF operational ensemble reanalysis–analysis system for ocean and sea ice: A description of the system and assessment. Ocean Sci., 15, 779–808, https://doi.org/10.5194/os-15-779-2019.

Tables

Table 1 CERES and ERA5 Southern Hemisphere (SH), Northern Hemisphere (NH) and Global ASR, −OLR and NET TOA flux average, monthly anomaly standard deviation (Stdev) and trend for 03/2000-02/2020. Numbers in parentheses correspond to uncertainty at 95% significance level. Bold indicates trend above 95% significance.

	CERES								
	ASR			−OLR			Net		
	SH	NH	Global	SH	NH	Global	SH	NH	Global
Mean (Wm^{-2})	241.0	240.9	241.0	–239.6	–240.9	–240.2	1.39	0.076	0.73
Stdev (Wm^{-2})	0.98	0.94	0.67	0.74	0.83	0.51	0.89	0.88	0.69
Trend (Wm^{-2} dec^{-1})	**0.65 (0.29)**	**0.72 (0.28)**	**0.68 (0.24)**	−0.27 (0.33)	**−0.26 (0.26)**	**−0.26 (0.24)**	**0.38 (0.32)**	**0.46 (0.27)**	**0.42 (0.23)**
	ERA5 Forecasts								
	ASR			-OLR			Net		
	SH	NH	Global	SH	NH	Global	SH	NH	Global
Mean (Wm^{-2})	242.2	243.4	242.8	−241.6	−242.7	−242.1	0.66	0.71	0.68
Stdev (Wm^{-2})	0.89	0.76	0.52	0.69	0.72	0.41	0.82	0.79	0.61
Trend (Wm^{-2} dec^{-1})	0.10 (0.29)	0.19 (0.24)	0.15 (0.24)	−0.11 (0.28)	−0.13 (0.22)	−0.12 (0.21)	−0.01 (0.29)	0.06 (0.26)	0.026 (0.25)
	IFS AMIP								
	ASR			-OLR			Net		
	SH	NH	Global	SH	NH	Global	SH	NH	Global
Mean (Wm^{-2})	239.6	242.0	240.1	-241.0	-241.7	-241.2	-1.4	0.34	-1.1
Stdev (Wm^{-2})	0.62	0.64	0.39	0.49	0.56	0.25	0.60	0.68	0.49
Trend (Wm^{-2} dec^{-1})	0.24 (0.25)	**0.28 (0.26)**	**0.26 (0.19)**	-0.019 (0.27)	-0.046 (0.24)	-0.034 (0.17)	0.22 (0.24)	0.24 (0.29)	0.23 (0.23)

Table 2 Average, standard deviation and trend for 03/2000-02/2020 in TEDIV and F_S for the SH, NH and global. Numbers in parentheses correspond to uncertainty at 95% significance level. Bold indicates trend above 95% significance.

	TEDIV								
	ERA5 Analysis			ERA5 Forecasts			IFS AMIP		
	SH	NH	Global	SH	NH	Global	SH	NH	Global
Mean (Wm^{-2})	-1.6	1.6	0.0	-5.8	-1.1	-3.4	-3.9	-0.13	-2.1
Stdev (Wm^{-2})	0.69	0.69	0.0	1.5	1.2	0.93	0.79	0.75	0.47
Trend (Wm^{-2} dec^{-1})	0.092 (0.15)	-0.092 (0.15)	0.0	0.32 (1.7)	**-0.87 (0.70)**	-0.27 (1.4)	0.003 (0.26)	0.039 (0.17)	0.022 (0.11)
	$\boldsymbol{F_S}$								
	Inferred			ERA5 Forecasts			IFS AMIP		
	SH	NH	Global	SH	NH	Global	SH	NH	Global
Mean (Wm^{-2})	3.0	-1.5	0.71	6.4	1.8	4.1	2.5	0.47	1.0
Stdev (Wm^{-2})	1.6	1.5	1.2	1.7	1.4	1.2	0.84	1.0	0.64
Trend (Wm^{-2} dec^{-1})	0.24 (0.35)	**0.55 (0.31)**	**0.40 (0.25)**	-0.38 (1.5)	**0.92 (0.69)**	0.27 (1.1)	0.22 (0.26)	0.20 (0.36)	**0.21 (0.21)**

Table 3 Mean, anomaly standard deviation and trend in monthly ocean heating rate during 03/2000-02/2020 for the SH, NH and global (total area). Numbers in parentheses correspond to uncertainty at 95% significance level. Bold indicates trend above 95% significance.

	ORAS5					
	0-700 m			Full Depth		
	SH	NH	Global	SH	NH	Global
Mean (Wm^{-2})	0.65	0.50	0.57	1.2	0.87	1.0
Stdev (Wm^{-2})	2.4	2.5	1.0	2.6	2.8	1.1
Trend (Wm^{-2} dec^{-1})	-0.11 (1.0)	-0.062 (0.98)	-0.086 (0.31)	-0.24 (1.1)	-0.13 (1.1)	-0.19 (0.47)
	ORAS6.1					
	0-700 m			Full Depth		
	SH	NH	Global	SH	NH	Global
Mean (Wm^{-2})	0.43	0.39	0.41	0.38	0.64	0.51
Stdev (Wm^{-2})	2.6	2.5	1.2	2.9	2.8	1.3
Trend (Wm^{-2} dec^{-1})	-0.11 (1.0)	0.13 (0.98)	0.009 (0.36)	0.013 (1.2)	0.31 (1.1)	0.16 (0.60)
	ORAS6-ctrl					
	0-700 m			Full Depth		
	SH	NH	Global	SH	NH	Global
Mean (Wm^{-2})	0.48	0.29	0.38	0.77	0.30	0.54
Stdev (Wm^{-2})	2.2	2.0	0.82	2.5	2.2	0.81
Trend (Wm^{-2} dec^{-1})	-0.10 (1.0)	0.022 (0.87)	-0.038 (0.38)	0.037 (1.1)	-0.026 (0.95)	0.006 (0.38)

Table 4 Mean, standard deviation and trend in annual ocean heating rate during 07/2005-12/2019 for the SH, NH and global (total area). Numbers in parentheses correspond to uncertainty at 95% significance level. Bold indicates trend above 95% significance.

	ORAS5					
	0-700 m			Full Depth		
	SH	NH	Global	SH	NH	Global
Mean (Wm^{-2})	0.54	0.38	0.46	1.1	0.65	0.88
Stdev (Wm^{-2})	1.3	1.3	0.40	1.4	1.4	0.45
Trend (Wm^{-2} dec^{-1})	0.15 (1.2)	0.56 (1.2)	0.36 (0.55)	-0.37 (1.3)	0.84 (1.3)	0.24 (0.70)
	ORAS6.1					
	0-700 m			Full Depth		
	SH	NH	Global	SH	NH	Global
Mean (Wm^{-2})	0.30	0.34	0.32	0.26	0.67	0.46
Stdev (Wm^{-2})	1.2	1.3	0.45	1.4	1.4	0.59
Trend (Wm^{-2} dec^{-1})	0.42 (1.2)	0.85 (1.2)	**0.63 (0.53)**	0.87 (1.4)	1.1 (1.3)	**0.98 (0.67)**
	ORAS6-ctrl					
	0-700 m			Full Depth		
	SH	NH	Global	SH	NH	Global
Mean (Wm^{-2})	0.43	0.33	0.38	0.78	0.33	0.55
Stdev (Wm^{-2})	1.3	1.1	0.45	1.4	1.2	0.44
Trend (Wm^{-2} dec^{-1})	0.31 (1.3)	0.35 (1.1)	0.33 (0.64)	0.23 (1.4)	0.34 (1.2)	0.28 (0.67)
	Argo					
	0-700 m			Full Depth		
	SH	NH	Global	SH	NH	Global
Mean (Wm^{-2})	0.45	0.23	0.34	0.77	0.40	0.60
Stdev (Wm^{-2})	2.2	2.1	0.76	3.0	2.3	1.2
Trend (Wm^{-2} dec^{-1})	-0.049 (2.1)	1.2 (2.0)	0.49 (0.72)	-0.22 (3.0)	1.4 (2.2)	0.46 (1.2)
	Argo+SA					
	0-700 m			Full Depth		
	SH	NH	Global	SH	NH	Global
Mean (Wm^{-2})	-	-	-	0.76	0.41	0.59
Stdev (Wm^{-2})	-	-	-	1.0	1.0	0.37
Trend (Wm^{-2} dec^{-1})	-	-	-	0.11 (1.6)	0.74 (1.6)	0.42 (0.44)

921

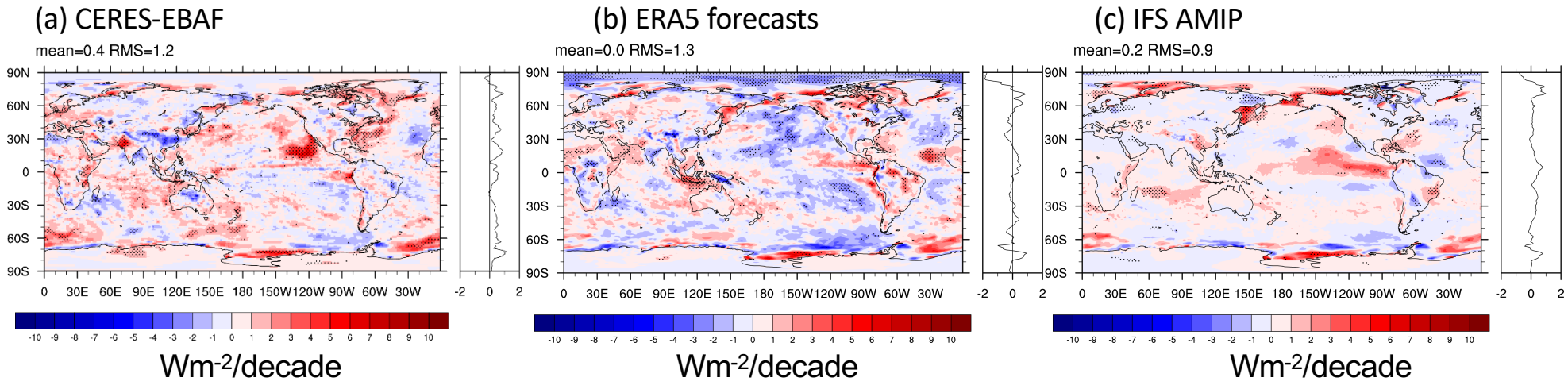

Figure 1 Trends in TOA Net Radiation for 2000/03-2020/02. (a) CERES-EBAF, (b) ERA5 forecasts and (c) IFS AMIP.

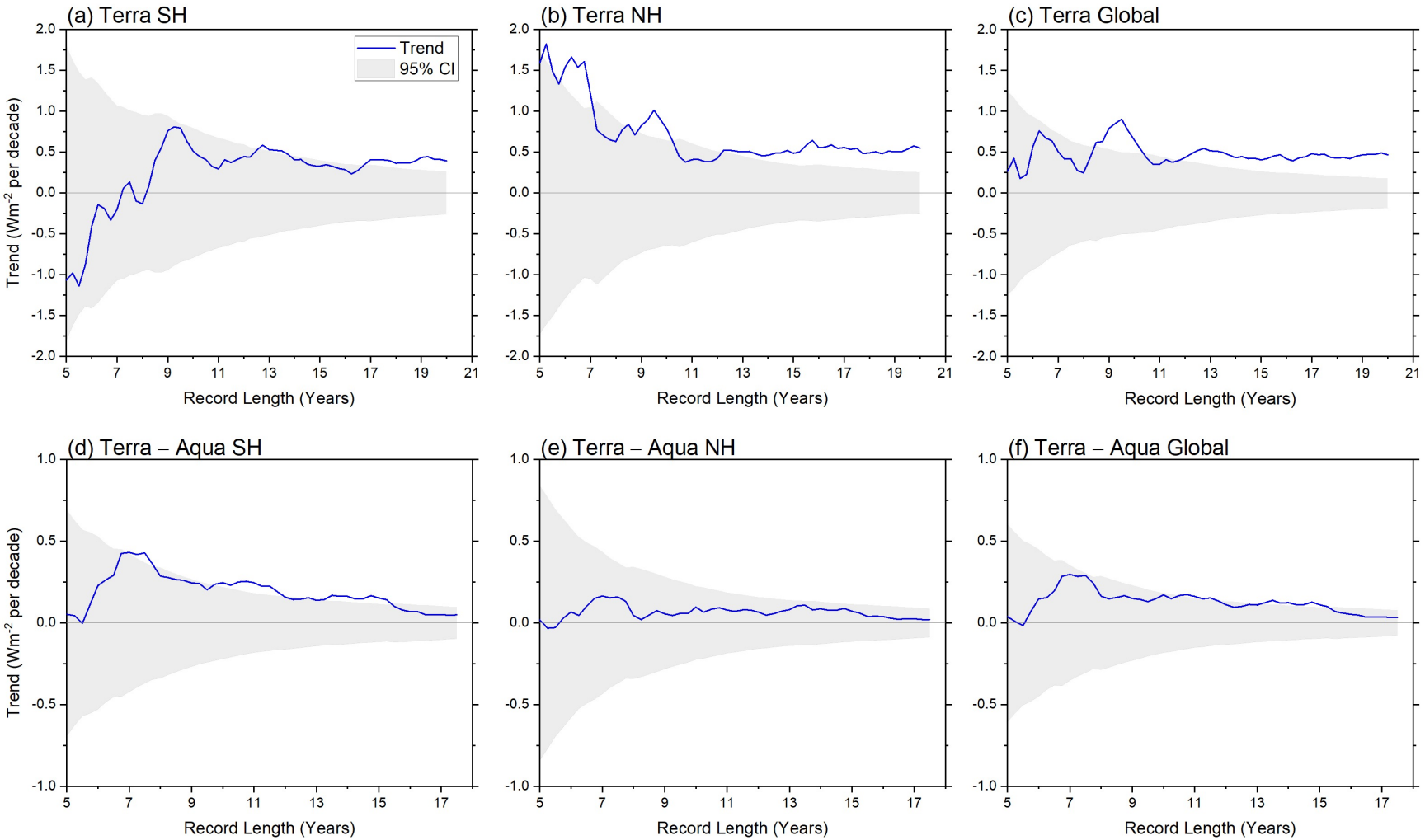

Figure 2 CERES net TOA flux trends against record length for CERES SSF1deg Terra (top) and Terra – Aqua (bottom) for (a, d) SH, (b, e) NH, (c, f) Global. Start date is 03/2000 for Terra and 07/2002 for Terra – Aqua. Gray shading corresponds to 95% confidence interval.

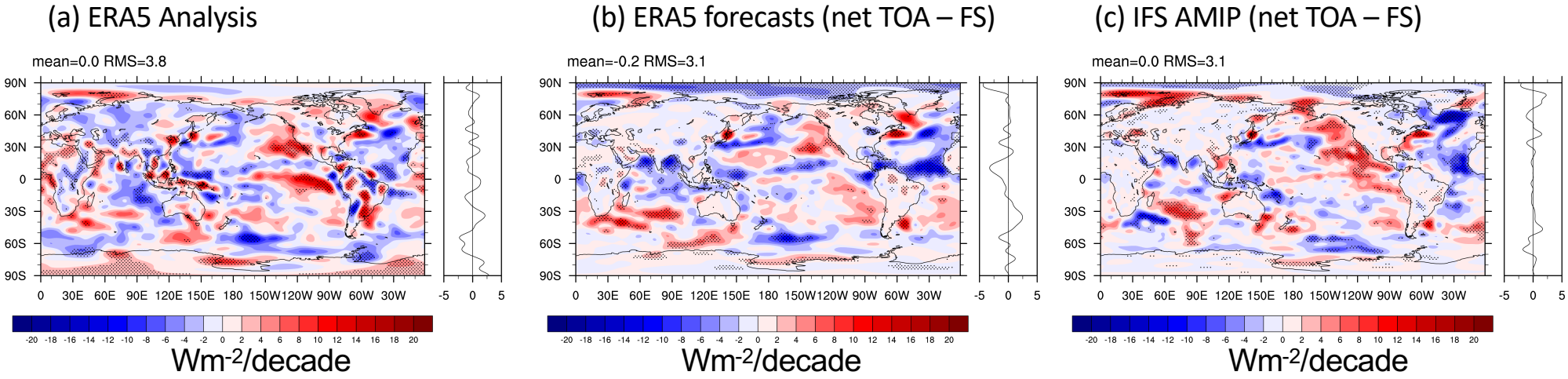

Figure 3 Trends in vertically integrated divergence of total atmospheric energy transport (TEDIV) for 2000/03-2020/02. (a) ERA5 Analysis (directly from wind, T, q etc), (b) ERA5 forecasts (net TOA – FS) and (c) IFS AMIP (net TOA – FS).

.

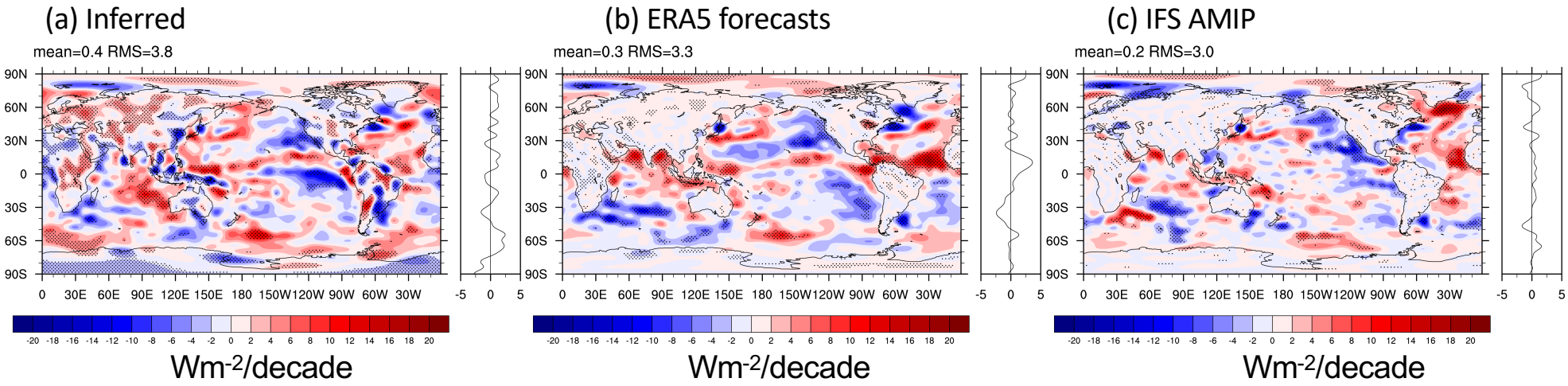

Figure 4 Trends in surface flux (positive downward) for 2000/03-2020/02. (a) Inferred (CERES TOA Net − ERA5 TEDIV), (b) ERA5 forecasts and (c) IFS AMIP.

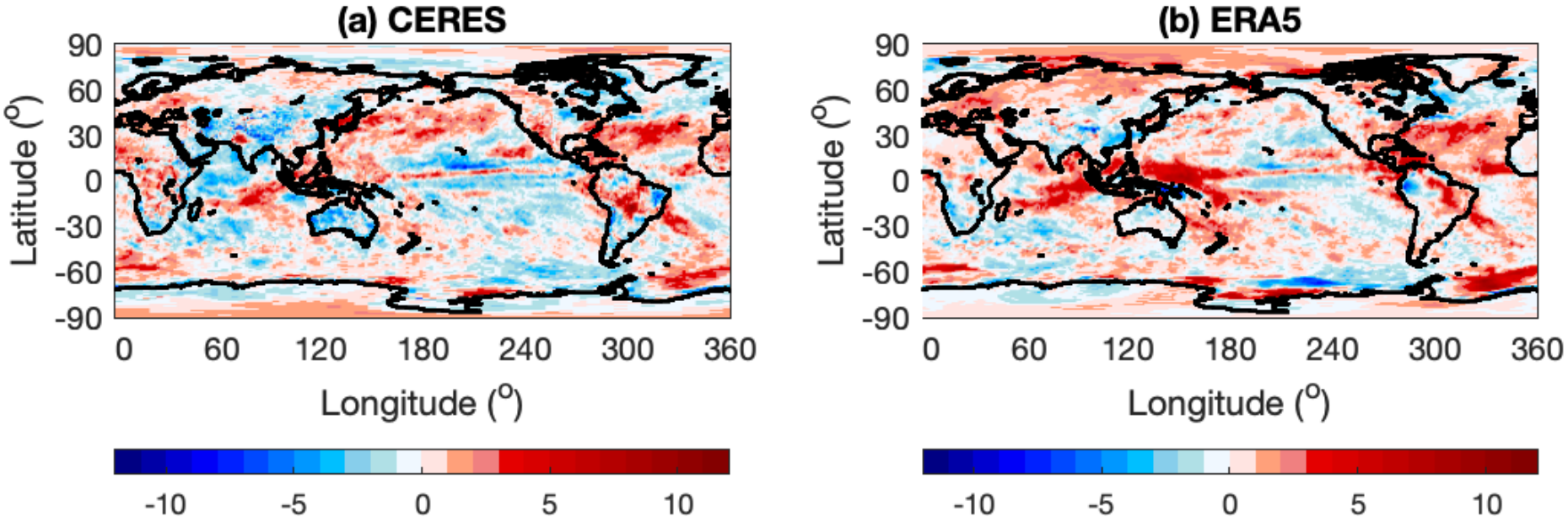

Figure 5 Trend for 200208-202002 in net total radiative flux at the surface (positive down) from (a) CERES and (b) ERA5 forecasts.

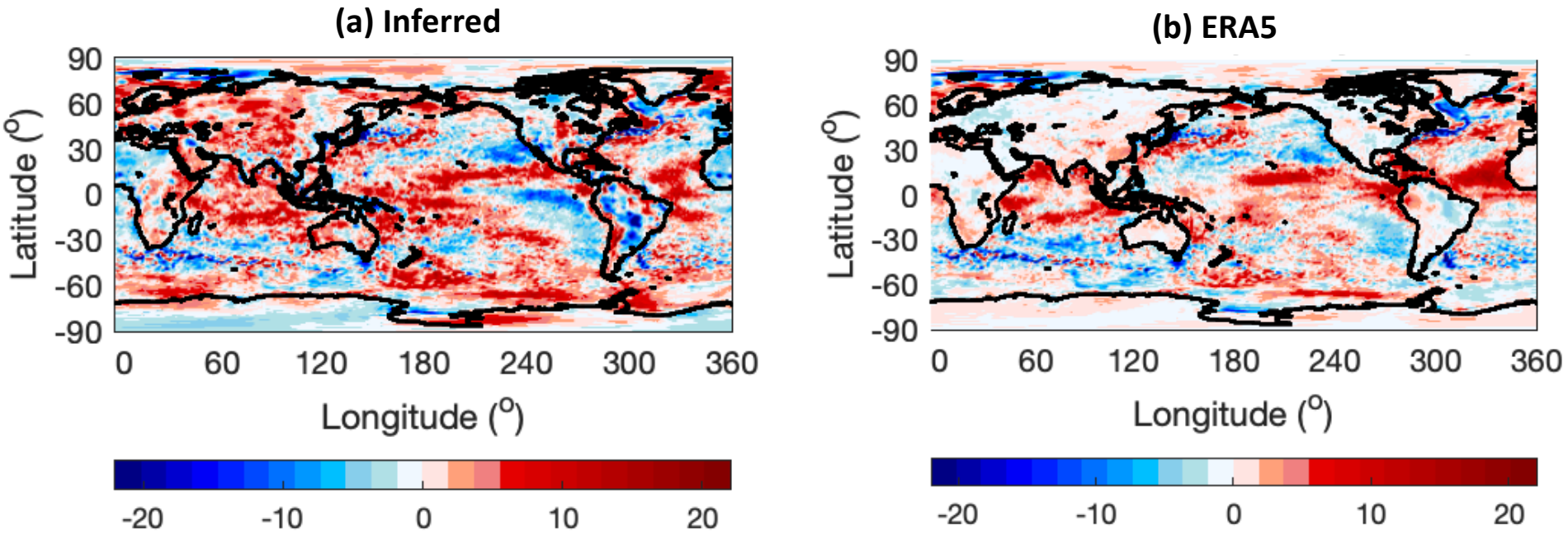

Figure 6 Trends in surface turbulent heat flux (positive downward) for 2002/08-2020/02. (a) Inferred (CERES TOA Net − ERA5 TEDIV − CERES Surface Net) and (b) ERA5 forecasts.

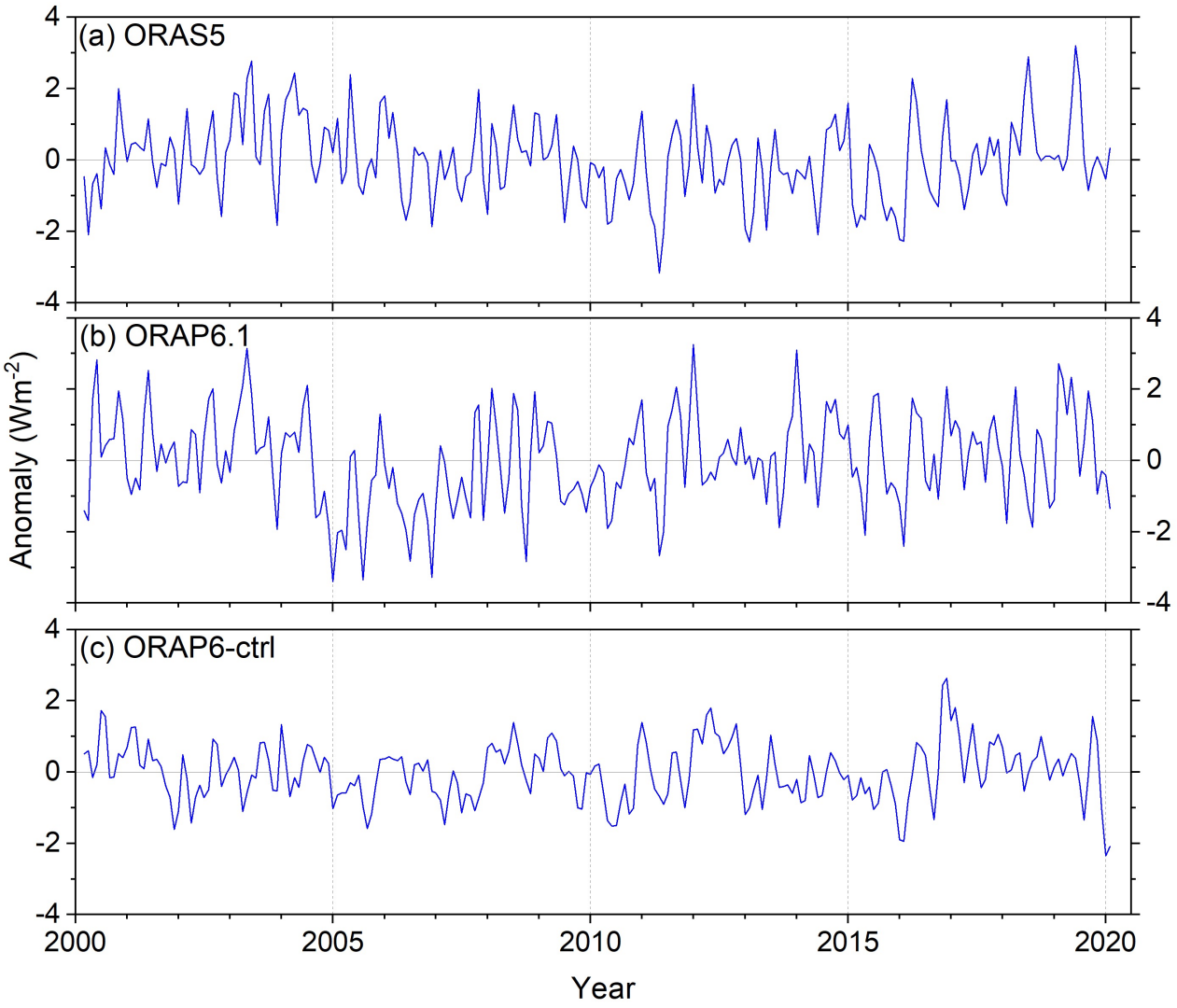

Figure 7 Monthly anomalies in ocean heating rate for (a) ORAS5, (b) ORAP6.1, (c) ORAP6-ctrl.

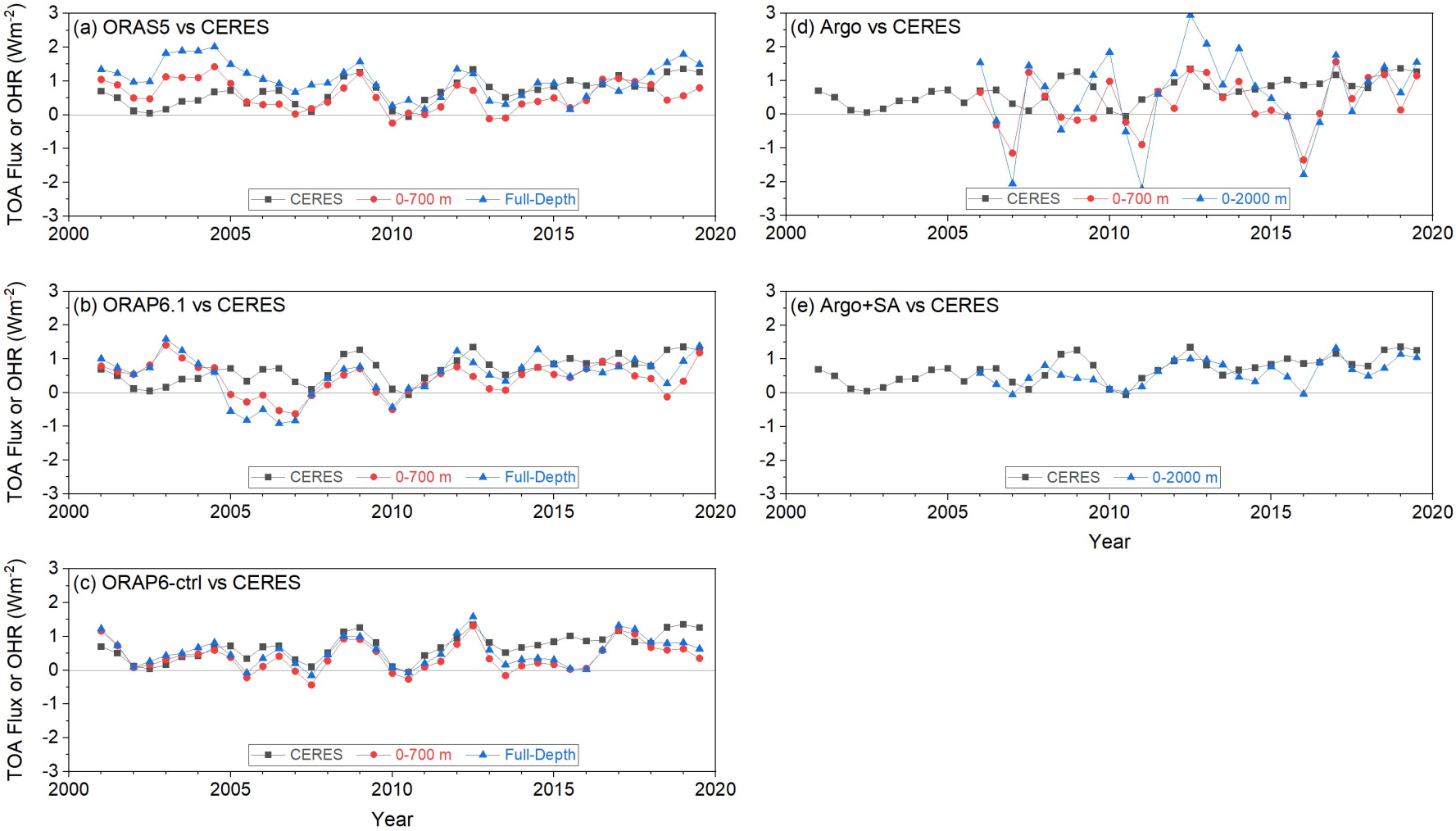

Figure 8 Global annual mean variation in CERES net TOA flux and ocean heating rate for 0-700 m and full-depth or 0-2000 m for: (a) ORAS5; (b) ORAP6.1; (c) ORAP6-ctrl; (d) Argo; (e) Argo+SLA.